Article:
Graham, S.J. orcid.org/0000-0002-1296-1680, Gallagher, E. orcid.org/0009-0002-8091-4904, Baxter, G.J. orcid.org/0009-0007-5037-6195 et al. (8 more authors) (2024) Powder production, FAST processing and properties of a Nb-silicide based alloy for high temperature aerospace applications. Journal of Materials Research and Technology, 28. pp. 3217-3224. ISSN 2238-7854

https://doi.org/10.1016/j.jmrt.2023.12.190

Journal of Materials Research and Technology 28 (2024) 3217–3224

Contents lists available at ScienceDirect

Journal of Materials Research and Technology

journal homepage: www.elsevier.com/locate/jmrt

Powder production, FAST processing and properties of a Nb-silicide based alloy for high temperature aerospace applications

Simon J. Graham [a], Edward Gallagher [a], Gavin J. Baxter [a], Yunus Azakli [a], Joseph Weeks [a], Matthew Gelmetti [a], Neil D'Souza [b], Carl Boettcher [b], Bryan Roebuck [c], Panos Tsakiropoulos [a], Claire Utton [a,*]

[a] University of Sheffield, Dept. of Materials Science and Engineering, Mappin Street, Sheffield, S1 3JD, United Kingdom
[b] Rolls-Royce plc, PO Box 31, Derby, DE24 8BJ, United Kingdom
[c] National Physical Laboratory, Hampton Road, Teddington, Middlesex, TW11 0LW, United Kingdom

ARTICLE INFO

Keywords:
Niobium silicide based alloys
Refractory metal intermetallic composites
Field assisted sintering technology
Spark plasma sintering
Mechanical properties

ABSTRACT

A Nb-silicide based alloy with nominal composition Nb–18Ti–22Si–6Mo-1.5Cr–2Sn-1Hf (at. %), designed for high temperature aerospace applications, was produced via a powder metallurgy (PM) route. The raw elements were arc melted, crushed, and milled to powder, then consolidated using Field Assisted Sintering Technology (FAST). The compressive creep of the alloy was evaluated using electro-thermal mechanical testing (ETMT). The study demonstrated the production of larger 60 mm diameter samples, with potential for further scale up. The microstructure of the FAST alloy, which is comprised of bcc Nb_{ss} and tetragonal αNb_5Si_3 was more homogenous compared with the cast alloy, with some interstitial contamination that occurred during powder production. The FAST alloy had lower density than state of the art Ni-based superalloys and refractory metal complex concentrated alloys (RCCAs) and high entropy alloys (RHEAs), and its yield strength and specific yield strength was higher than those of the latter metallic Ultra high temperature materials (UHTMs) and comparable to those of Nb-silicide based alloys with B addition. The stress exponent n in compressive creep was in the range 1.7–2.6, similar to that of binary Nb–10Si and Nb–16Si alloys and its creep rate at 1200 °C and 100 MPa was similar to that of the MASC alloy (Nb–25Ti–16Si-8Hf-2Al–2Cr (at.%)). Like the latter, the creep of the FAST alloy did not meet the creep goal.

1. Introduction

To improve the performance of gas turbine engines the turbine entry temperature (TET) must be increased to around 1850 °C. Efficiency can also be improved by reducing the overall weight of components (increasing the thrust to weight ratio). New metallic ultra-high temperature materials (UHTMs) are required that (i) have lower densities than conventional Ni-based superalloys, (ii) can withstand higher operating temperatures and (iii) meet property goals for toughness, creep and oxidation resistance [1]. Candidate metallic UHTMs are refractory metal (RM) intermetallic composites (RMICs), refractory metal high entropy alloys (RHEAs) and refractory metal complex concentrated alloys (RCCAs) [2].

RMICs based on Nb, i.e., RM(Nb)ICs, also known as Nb-silicide based alloys or Nb-silicide in situ composites, are composed of Nb solid solution (Nb_{ss}) and intermetallics (e.g. Nb_5Si_3, Nb_3Si, C14–$NbCr_2$ Laves phase and A15 compounds, e.g., Nb_3Sn, Nb_3Al, Nb_3Si), currently are explored as next generation metallic UHTMs to be used in the hottest parts of a turbine engine [1]. Some of the RM(Nb)ICs also satisfy (comply with) the definition of RCCAs or RHEAs, i.e., they are RM(Nb)ICs/RCCAs or RM(Nb)ICs/RHEAs. These alloys can have high melting temperatures in excess of 1750 °C, excellent high temperature mechanical properties, and lower densities (e.g. between 6.5 and 7.9 g/cm^3) than Ni-based superalloys [1,3]. The room temperature fracture toughness and oxidation resistance of Nb-silicide based alloys has been improved through alloy design and the use of specific alloying elements [1]. Like the Ni-based superalloys, the metallic UHTMs will need the protection offered by environmental coatings [4]. Unlike the Ni-based superalloys, the microstructures of metallic UHTMs are susceptible to interstitial contamination [5], in particular the bcc solid solution [6].

* Corresponding author.
E-mail address: c.utton@sheffield.ac.uk (C. Utton).

https://doi.org/10.1016/j.jmrt.2023.12.190
Received 4 August 2023; Received in revised form 20 December 2023; Accepted 21 December 2023
Available online 23 December 2023

Interstitial contamination, which can have a significant effect on the properties of RMICs, RHEAs and RCCAs, imposes constraints on alloy design and processing [1].

Manufacture and upscale of Nb-silicide based alloys is a known challenge for these materials [1]. Alloys can be produced using conventional casting methods using cold hearths, for example arc-melting or plasma melting with water-cooled Cu crucibles or directional solidification [1,7,8]. However, these methods result in compositional variation across the ingot, macrosegregation of solute additions [9], heterogeneous microstructure and casting defects such as cracks and pores [7]. Advanced manufacturing methods have been proposed to overcome these issues and allow greater control over the microstructure. More recently, powder metallurgy (PM) techniques, including Field Assisted Sintering Technology (FAST), also known as Spark Plasma Sintering (SPS), have been used to produce small amounts of Nb-silicide based alloys, however the volume of published research is relatively limited. Furthermore, interstitial contamination in FAST processing of Nb-silicide based alloys has not received the focus it deserves, as is the general case for the processing of these alloys [1].

FAST is an effective sintering method for many different powdered materials, including metals and alloys [8,10]. It is capable of consolidating to very high densities whilst requiring relatively low temperatures and processing times compared with Hot Isostatic Pressing (HIP). This is due to simultaneous application of heat and pressure, along with rapid heating rates. FAST is therefore a suitable technique for the production of Nb-silicide based alloys from powders and has been shown to give fully dense material whilst eliminating casting defects and generating a more refined microstructure [7,11,12].

Several different approaches to producing Nb-silicide based alloys using FAST have been investigated in previous studies [7,11–13]. Blends of the necessary elemental powders have been used to generate alloys via reactive sintering, although this is difficult to control, due to the differing melting temperatures in multicomponent systems, especially in those with the addition of other RMs such as Mo, Ta or W, and sluggish reaction kinetics [14]. Instead, for binary Nb–Si alloys mixtures of Nb and Nb_5Si_3 powders have been used to overcome the lower melting point of Si. However, for multicomponent alloy systems with RMs and other low melting point elements, e.g., Al and Sn, the use of pre-alloyed powders is preferred [3,7]. Pre-alloyed powders can be produced using different manufacturing techniques. Mechanical alloying or comminution of either arc melted ingots or pre-sintered elemental powders via ball milling have been used on smaller scales [7,11], whereas inert gas atomisation has been used at larger scales [3,12,13,15].

The limited published literature on FAST of Nb–Si alloys relates to manufacture of samples typically less than 20 mm in diameter [7,11,12]. The capabilities of FAST are continually increasing, with the largest machines now capable of producing parts up to 600 mm in diameter, highlighting that further scale up is already possible [16]. The refined and more homogeneous microstructures generated via this powder-based route are expected to provide improved and more consistent properties than from casting alone, whilst eliminating defects. This is crucial for materials in critical components, where properties such as fatigue performance are dependent on a homogeneous, defect free microstructure. Larger scale FAST will allow for more representative mechanical property studies to be conducted, for example to assess tensile and compressive properties at elevated temperatures using electro-thermal mechanical testing (ETMT). Furthermore, data about interstitial contamination of PM Nb–Si alloys is lacking even though interstitials are known to affect phase stability and mechanical properties [1,6,17].

In this study, samples up to 60 mm in diameter of Nb-silicide based alloy with nominal composition Nb–18Ti–22Si–6Mo-1.5Cr–2Sn-1Hf (at. %) were produced through a processing route of arc melting, ball-milling, and FAST consolidation. The composition was chosen to give a good balance of high temperature mechanical properties and oxidation resistance. Cr, Hf, Mo, Sn, Ti partition to the Nb_{ss} and provide solid solution strengthening, in particular Mo and Ti, whilst Ti and Hf partition to the Nb_5Si_3. Ti also improves oxidation resistance, reduces density, and improves fracture toughness [8,18]. Si was added to form the desirable Nb_5Si_3 silicide. This can be a tetragonal phase (tI32) which can have both a high temperature stable βNb_5Si_3 phase (prototype W_5Si_3) and low temperature stable αNb_5Si_3 phase (prototype Cr_5B_3) [17]. Metastable γNb_5Si_3 (hexagonal hP16, Mn_5Si_3 prototype) can be stabilised by carbon contamination [17] and by high Ti and Hf concentrations in the silicide, resulting in $Nb/(Ti + Hf) < 1$ [18,19]. Furthermore, it was expected that Cr, Sn and Hf additions would improve the oxidation resistance, in particular Hf which scavenges oxygen [18] and decreases the diffusivity of oxygen towards the bulk of Nb-silicide based alloys and thus is expected to be effective regarding control of contamination with oxygen [20].

This paper presents the results of an initial study of process-microstructure relationships for the aforementioned alloy, as well as assessing mechanical properties through hardness measurements and electro-thermal mechanical testing (ETMT).

2. Methods

High purity pieces of Nb (99.8 %), Ti (99.99 %), Si (99.999 %), Mo (99.95 %), Cr (99.99 %), Sn (99.99 %) and Hf (99.9 %) were weighed out based on the alloy composition. An Arcast Arc 200 arc melter with non-consumable tungsten electrode was used to melt the elements together in a water cooled copper crucible. The melting chamber was pumped down to a vacuum of 5×10^{-2} mbar and flushed with argon two times before achieving the ultimate vacuum level of 4×10^{-5} mbar. Then, the chamber was backfilled with argon to about 700 mbar before melting. Arc melting was done in two stages to avoid severe vaporisation of elements with high vapour pressure, with the ingots being flipped and re-melted six times in each stage to ensure best possible chemical homogeneity of the alloy. In the first stage, the elements with higher melting point (Nb, Ti, Mo, Cr and Hf) were melted together, then Si and Sn were added in the second stage. Extra Si, Sn and Cr were added to compensate for their loss due to vaporisation during arc melting. Several button ingots were produced for further processing, each approximately 100 g in mass and around 45 mm in diameter. Different stages of the processing of the Nb-silicide based alloy of this study are shown in Fig. 1.

The ingots were initially crushed using a percussion mortar. The crushed particulate material was then placed into a zirconia-lined jar, along with zirconia grinding balls, fitted with an aeration lid and flushed with argon to create an inert atmosphere. A Retsch PM100 planetary ball mill was used to grind the material to a powder under the inert conditions. Individual ingot crushed and ground powders were combined to create a single powder blend. The powder was sieved to <250 μm and the resulting particle size distribution (PSD) was measured by laser diffraction using a Malvern Mastersizer 3000.

Initial FAST processing was carried out using 10 g of the alloy powder blend to produce 20 mm diameter samples. The FAST parameters that were optimised at the small scale subsequently were used to produce a sample of 60 mm diameter and 4.5 mm thickness, using 90 g of the powder. The powder was placed into a 60 mm internal diameter graphite mould, lined with graphite foil that was removed after processing. A graphite felt jacket was used around the tooling for thermal insulation to prevent heat loss and improve power efficiency. FAST processing was done using an FCT Systeme HP D 25 type furnace, where the temperature was measured using a pyrometer. The sample was heated at 150 °C min^{-1} up to 1300 °C, then at 75 °C min^{-1} to a maximum temperature of 1500 °C, at which point a pressure of 50 MPa was applied and held for 5 min. The entire test was performed under a vacuum of 5×10^{-2} mbar. After cooling to room temperature, the sample was removed from the graphite tooling, and the surface was cleaned using abrasive grit blasting.

The as cast ingot, milled powder and FAST consolidated material were studied to understand the microstructural evolution and any

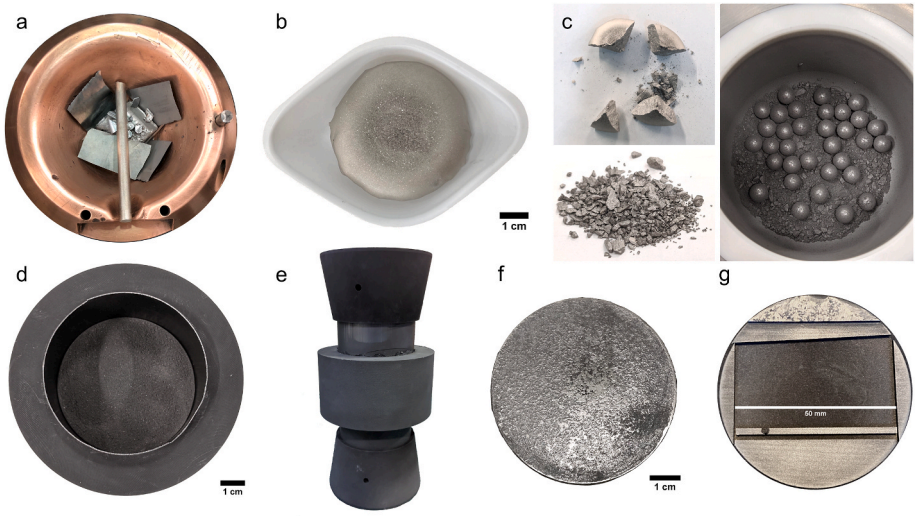

Fig. 1. a) Elements in copper crucible prior to arc melting, b) resulting ingot, c) stages of powder production from ingot, using a percussion mortar and ball milling, d) alloy powder in 60 mm internal diameter FAST mould, e) FAST tooling assembly which sits between two electrodes, f) 60 mm FAST sample produced after abrasive grit blasting, g) FAST sample after ETMT specimen extraction via EDM, with example specimen.

changes in chemistry during processing. The bulk chemistries of the powder blend and FAST samples were measured using inductively coupled plasma - optical emission spectroscopy (ICP-OES, for alloying elements), inert gas fusion (oxygen and nitrogen, Eltra ONH 2000), and combustion analysis (carbon). Measurement error is approximately ±10 at.%. Phases in the bulk as cast ingot and FAST sample were identified using a Bruker D2 phaser x-ray diffraction (XRD) machine (Cu radiation (30 kV, 10 mA), 0.02° step) and ICDD database. One of the ingots and a section of the FAST sample were sectioned using a diamond cutting wheel, then polished by metallographic preparation consisting of a range of SiC grinding papers, followed by 0.06 μm colloidal silica solution. An FEI Inspect F50 scanning electron microscope (SEM) and Oxford Instruments energy dispersive X-ray spectroscopy (X-EDS) detector were used to analyse the microstructure. Vickers hardness was measured on the polished surfaces using a Struers Durascan-80. A grid of 16 indents covering an area of 8 mm^2 was tested, with a force of 1 kg (HV 1) applied for 15 s for each indent.

Electrical discharge machining (EDM) was used to extract 3 x 1 × 50 mm matchstick specimens from the FAST consolidated material for ETMT. The density of the alloy was measured using the Archimedes method, with a mean average value taken from two of the matchstick specimens.

An ETMT system developed at the National Physical Laboratory was used to measure the macroscopic stress, while the plastic strain is calculated by monitoring changes in resistance. More details of the experimental set-up can be obtained from Refs. [21–25]. This ETMT system also is used to assess the mechanical behaviour of Ni-based superalloys [24]. The true plastic strain, ε^{pl}, was measured according to the change in resistance between the central gauge length of the test piece where the temperature profile is approximately uniform (± 5 K). The measurement resolution is determined by the type of thermocouple used t.o measure temperature, in this case Pt/Pt–13%Rh and is less than 1 K at 1573 K (1300 °C). In Ni-base superalloys, the individual resistivity of the γ and γ′ phases differ at any temperature (resistivity of γ′ being greater than that for γ phase) and therefore the temperature dependence of resistivity arises from the relative volume fraction of γ and γ′, irrespective of the application of load [22]. Since dissolution of γ′ occurs during heating, there will be a concomitant change in resistivity (and resistance) with temperature arising from the phase transformation. Consequently, in the case of applied load, R is the measured resistance and R_0 is the strain-free resistance for zero-load, equation (1) is used to calculate the plastic strain, ϵ^{pl} [22,23]:

$$\epsilon^{pl} = \frac{1}{2}\ln\left(\frac{R}{R_0}\right) \tag{1}$$

In miniature testing, the gauge volume can be used to assess location specific properties. The gauge length here is determined by the distance between which resistance is measured; approximately L = 2.75 mm at room temperature for Ni-alloys [26–28]. During heating, the sample gauge length will increase, though this is small and therefore no correction is needed. Indeed, in the case of Nb-silicide based alloys, the strain increase $\varepsilon = \alpha\,\Delta T \ll 1$, where the thermal expansion coefficient $\alpha = 7.3 \times 10^{-6}\ K^{-1}$ and $\Delta T \approx 1300$ K. The gauge length at any temperature is L ~2.75 mm and therefore constant over the entire temperature range. The gauge volume is therefore typically about 5.5–11 mm^3.

The variation of resistivity with temperature, ρ_T can be calculated via;

$$\rho_T = R_T\left(\frac{A}{L}\right) \tag{2}$$

where R_T is the ETMT measured resistance at temperature *T,* and *A* is the cross-section area.

Since the plastic strain is measured from the resistance, any error in the resistance measurement contributes to an error in the plastic strain. The current and voltage measurements are made with better than 1 part in 10^4 uncertainty and the maximum range in the measured resistance is ±0.002 mΩ and with an accompanying standard deviation of ±0.001 mΩ. From Equation (1), the upper and lower plastic bounds of plastic strain is given by; $\varepsilon^{pl} = \frac{1}{2}\ln\left(\frac{R\pm\Delta R}{R_0\pm\Delta R_0}\right)$. This is used to estimate a plastic strain resolution of about 0.05 %.

Compressive creep tests were carried out on matchstick specimens. The length of each specimen was 50 mm, while the gauge length (isothermal to within ± 3K between 1000 °C and 1200 °C was between 2.7 and 3 mm). The width and thickness of the specimens varied between 1.27 to 3 mm and 0.79–0.98 mm, respectively. The sample was heated under zero-load to the set temperature and a number of interrupted creep tests were carried out by stepping the load. The primary purpose for carrying out such stepped creep tests was to be able to obtain creep data over a range of stresses at a given temperature and thus obtain a steady-state creep rate, as this approach is sample economic. A similar approach has been adopted before [26]. To identify any history dependence of prior deformation (at the previous stress/temperature)

on the creep rate at the next successive stress/temperature, a specimen was first heated to 1050 °C and a set of creep tests carried out, before heating to 1200 °C and carrying out some more creep tests. This will be referred to in the next section as the first creep test. The reverse was also done, i.e., another specimen was first heated to 1200 °C and a set of creep tests carried out, before cooling to 1050 °C and carrying out further creep tests.

3. Results and discussion

3.1. Blended Nb-silicide based alloy powder

Table 1 shows that there was good agreement between the nominal composition, ingot composition, and that of the powder blend. During the initial arc melting trials, vaporisation led to significant variation in the composition, and so a few iterations were completed using different amounts of some elements to achieve a chemical composition as close as possible to the nominal one. Despite this, the actual composition of the ingots did not match exactly the nominal alloy composition. This accounts for the variation between the ingot compositions and powder blend, as the powder blend was the average of several combined ingots.

Interstitial elements can impact the mechanical properties of RMs, alloys with RM additions [1] and their phases [6]. The maximum solid solubility of oxygen in Nb is 9 at.% at 1915 °C and about 6 at.% at 1500 °C [29]. The effect of solute elements in the solid solutions in Nb silicide based alloys on the maximum solid solubility of oxygen is not known [6], and the same is the case for the Nb_{ss} of the alloy in this study. Contamination with oxygen of the bcc solid solution affects its hardness and Young's modulus [6]. The Nb_5Si_3 can also be contaminated with oxygen, however its contamination is less severe compared with the Nb_{ss} [30] and affects the hardness and Young's modulus of the silicide. The bcc solid solution in RM(Nb)ICs is their Achilles' heel as it provides the path for interstitials to contaminate their microstructure [6]. Control of interstitials during processing is challenging as contamination can occur from several sources, including milling media and container, milling environment and tooling [1]. Interstitial pickup occurred during the processing, with a significant increase in oxygen content in the powder blend compared with the ingot, revealing that the majority of the increase in oxygen content occurred during the crushing and ball milling of the material. The oxygen content given in Table 1 is a bulk measurement, and therefore the oxygen content of individual phases is not reported. The increase in bulk oxygen content could have been caused by contamination from the ZrO_2 milling media, although it is more likely from reaction with atmospheric oxygen. This suggests that the argon flushing of the milling container was not sufficient, however more investigation is required to confirm this. Heat generated during milling could also enhance pickup of oxygen. The increase in oxygen content can affect mechanical properties and change phase equilibria where contamination is high [31]. Therefore, it is important to both minimise and quantify the extent of contamination during processing, to assess the impact on properties.

Table 1
Chemistry of nominal composition compared to one ingot and powder blend.

Element	Nominal (at.%)	Ingot (at.%)	Powder blend (at.%)
Nb	49.5	50.2	47.5
Si	22	22.5	21.9
Ti	18	17.2	19
Mo	6	5.6	5.9
Sn	2	1.8	1.8
Cr	1.5	1.3	1.1
Hf	1	0.9	1.0
C	–	0.05	0.04
O	–	0.3	1.5
N	–	0.2	0.2
TOTAL	100	100	100

The particle size distribution (PSD) of the powder was measured after milling and sieving, with the results displayed in Fig. 2. Although sieved to <250 μm, the D_{90} was <100 μm, indicating that the milling process was effective in producing a fine powder from the ingots, but some larger particles remained. With greater understanding of the milling process, the PSD could be tailored to achieve a specific PSD.

SEM analysis of the blended powder (Fig. 3a) showed an expected large variation in both the particle size and morphology. Particles exhibited irregular morphology resulting from the milling, with fine particles adhering to the surfaces of the larger particles, a feature that is common also with gas atomised particles where "satellite" fine powder particles adhere to larger particles. The backscattered electron micrograph of the polished cross section of powder particles in Fig. 3b reveals the microstructures and phases present: Nb_5Si_3 and Nb_{ss} (brighter Z contrast). The area fraction of each phase varied between different powder particles and also depended on powder particle size owing to the heterogeneous microstructure of the as cast ingots. There was no evidence of HfO_2 particles in the microstructure of the as cast alloy and the powder particles after milling.

3.2. FAST consolidated Nb-silicide based alloy powder

Initial FAST parameters were chosen based on previous, small-scale, trials with similar alloy powder compositions [32]. Several 20 mm diameter samples were produced and studied to determine the optimal parameters required to achieve full density for the alloy of this study. It was determined that a temperature of 1500 °C, combined with a pressure of 50 MPa was sufficient to achieve full consolidation, with no remaining porosity visible. These conditions were again used but on a larger scale to create a 60 mm diameter sample (Fig. 1). This size would make it possible to extract specimens for the ETMT creep experiments.

After FAST consolidation, the content of interstitial elements was once again measured and compared with the powder, to determine any effect of the processing. There was no evidence of oxygen or N pickup (1.31 and 0.2 at.%, respectively), due to the FAST processing occurring under vacuum conditions. The C content can increase due to contamination from the graphite foil surrounding the sample during processing. In our experiments, the measured bulk C concentration increased from 0.04 to 0.09 at.% suggesting some pick up of C. It is expected that C will be concentrated at the surface of the sample, in contact with the graphite foil.

Bulk XRD data of the as cast and FAST material is given in Fig. 4. In the as cast alloy, both the αNb_5Si_3 and βNb_5Si_3 silicides were formed together with the bcc Nb_{ss}. In "large" as cast ingots of Nb-silicide based alloys the βNb_5Si_3 transforms to αNb_5Si_3 during solid state cooling [33,

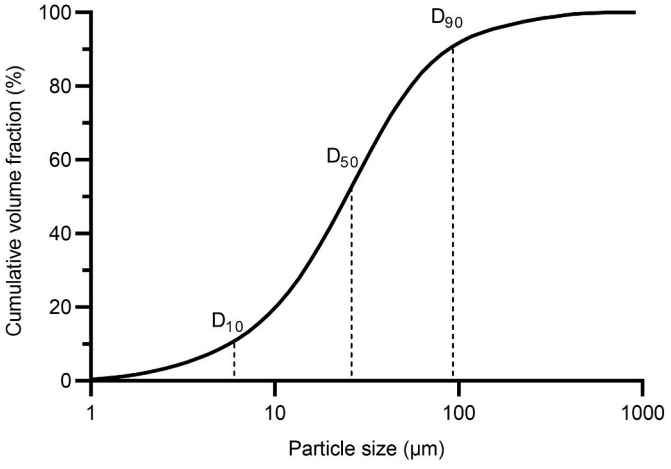

Fig. 2. Particle size analysis of Nb-silicide powder blend after sieving to <250 μm (D10 = 6.01 μm, D50 = 26.2 μm and D90 = 93.3 μm).

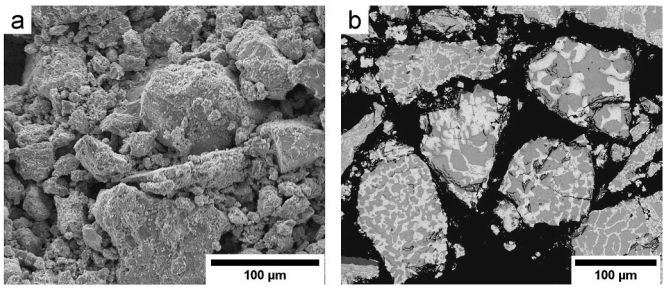

Fig. 3. Electron micrographs of powder blend a) secondary electron micrograph of powder blend b) backscattered electron micrograph of polished cross section of powder particles.

34]. In the cast alloy of this study the transformation of βNb_5Si_3 to αNb_5Si_3 must have started during solid state cooling, owing to the size of the ingot but was not finished owing to the Cr and Mo addition that tends to increase the stability of the βNb_5Si_3 (both Cr_5Si_3 and Mo_5Si_3 have the same prototype as βNb_5Si_3, namely W_5Si_3). Furthermore, hexagonal γNb_5Si_3 was not formed, which indicated that interstitial contamination of the microstructure was not severe and that the partitioning of Hf and Ti to Nb_5Si_3 did not result in Nb/(Ti + Hf) < 1 [17–19]. After FAST, the stable phases were bcc Nb_{ss} and the low temperature stable αNb_5Si_3 silicide. This suggests that the transformation of βNb_5Si_3 to αNb_5Si_3 was completed during FAST under these conditions. In addition, small peaks for HfO_2 were identified in the FAST sample. This correlates with the increased oxygen content of the material after milling, as the Hf acts as an oxygen scavenger, forming HfO_2. Furthermore, there was no evidence for γNb_5Si_3 in the FAST microstructure.

SEM and X-EDS were used to study the microstructure of the alloy after FAST processing, and to compare with the as cast ingot. The as cast microstructure (Fig. 5a and b) from the centre of the ingot, consisted of large Nb_5Si_3 regions surrounded by mixture of Nb_{ss} and Nb_5Si_3. There were some areas of eutectic consisting of these two phases, which were mostly formed adjacent to Nb_5Si_3 grains (seen in Fig. 5b). This would indicate that the solidification of the ingot started with the βNb_5Si_3 as the primary phase, followed by the formation of the Nb_{ss} and then of the Nb_{ss}+ βNb_5Si_3 eutectic. After milling and FAST consolidation, the microstructure changed considerably. The FAST microstructure appeared more homogeneous and refined, as expected from using powder. The large Nb_5Si_3 regions had been broken down during the milling process and so were much smaller in the FAST microstructure. There was still some variation in the scale and distribution of phases in the microstructure, as shown in Fig. 5d, resulting from the differences between the powder particles seen in Fig. 3b. Optimisation of the milling process and/or sieving to a smaller particle size would further improve microstructural homogenisation. Some porosity was observed, which is common in materials processed using PM, however this was measured to be <0.2 % following study of a mosaic of optical micrographs, and so not expected to have any significant impact on mechanical performance.

Elemental maps in X-EDS shown in Fig. 6 highlight how the different elements were segregated within the microstructure. As expected, Ti, Mo, Cr and Sn partitioned to the Nb_{ss}, whereas Si was present in the Nb_5Si_3 phase. A third phase is also seen in the FAST material, with X-EDS confirming this to be where the Hf is concentrated as HfO_2.

3.3. Hardness and creep behaviour of the NbSi based alloy

The hardness of the alloy, both as cast and after FAST processing, was measured as described in section 2. This made it possible to compare this alloy with other Nb-silicide based alloys and also to highlight the effect of differences in microstructural inhomogeneity on the hardness. Although both the as cast and FAST material exhibited similar mean hardness values, respectively 764 and 816 HV (Table 2), these were higher than the calculated with the alloy design methodology NICE [18] hardness (746 HV) for the nominal alloy composition. The range of values for the as cast alloy was significantly greater due to its more heterogeneous microstructure. The hardness of the Nb_5Si_3 silicide is significantly higher than that of the Nb_{ss}. Thus, large regions of Nb_5Si_3 lead to measuring high hardness value. In contrast, the FAST microstructure is more refined and homogeneous, and the indents sample a more representative microstructure. The maximum and minimum alloy hardness values in Table 2 are within the range of hardness that is typical of RM(Nb)ICs and RM(Nb)ICs/RCCAs. The measured density of the alloy after FAST processing was 7.12 g/cm^3. The density was lower than the density of latest generation Ni-based superalloys used in high pressure turbines in aero engines, in the range of values reported for RM (Nb)ICs [1] and significantly lower than the density of high strength RCCAs and RHEAs [35]. The room temperature yield strength of the alloy of this study calculated from hardness (σ_y = HV/3 – where hardness is in GPa) was 2497 and 2667 MPa, respectively for the as cast and

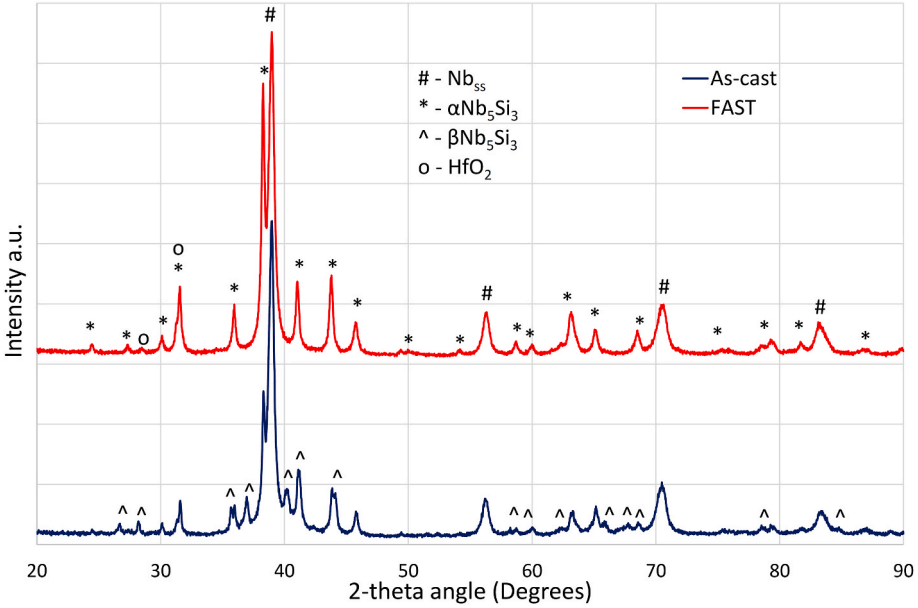

Fig. 4. XRD patterns of bulk as cast ingot and 60 mm FAST sample.

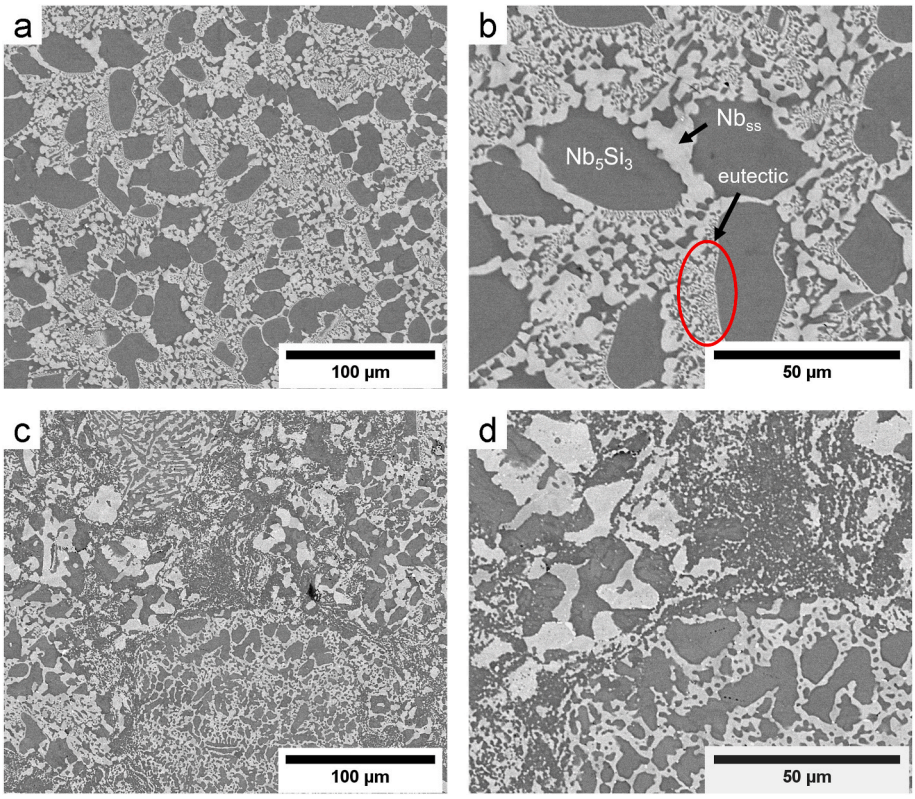

Fig. 5. Backscattered electron micrographs of as cast material from centre of ingot (a and b) and FAST consolidated material (c and d).

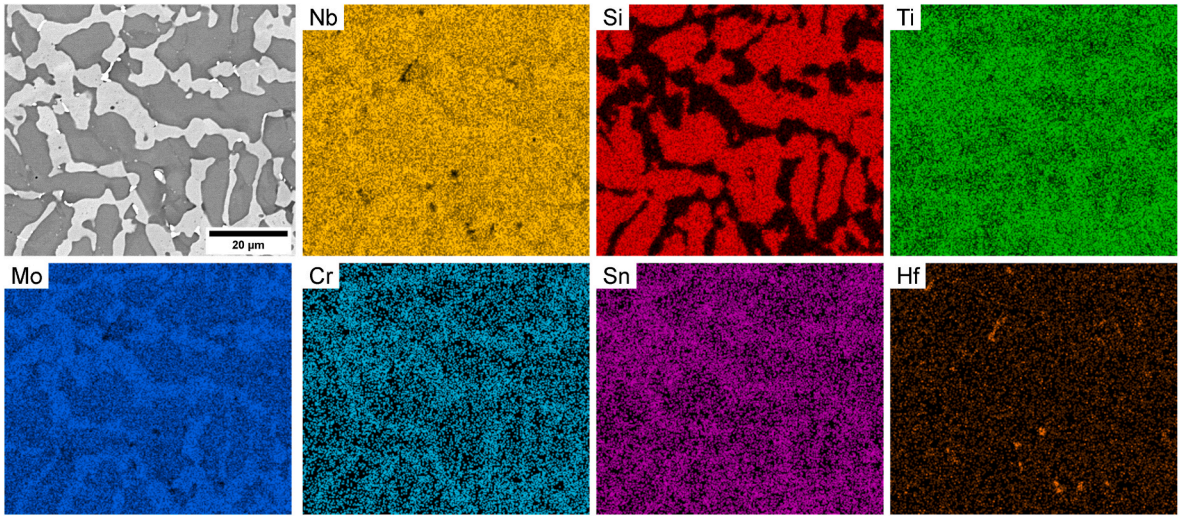

Fig. 6. Backscattered electron micrograph of FAST consolidated material, with corresponding X-EDS element maps.

Table 2
Comparison of Vickers hardness (HV 1) measured values for both as cast and FAST consolidated alloy.

Processing	Vickers Hardness (HV 1)			
	Minimum	Maximum	Range	Mean
as cast	674	957	283	764
FAST	746	903	157	816

FAST condition. For the latter, the yield strength was slightly higher than that of the RHEA nanocrystalline alloy MoNbTaVW (ρ = 12.29 g/cm^3) processed using SPS [35]. The room temperature specific yield strength calculated from hardness and the measured density was 351 and 375 MPa cm^3 g^{-1}, respectively for the as cast and FAST condition. For both conditions it was higher than that of the RHEAs and RCCAs reviewed in Ref. [35], in the range of values reported for B containing arc cast RM(Nb)ICs, RM(Nb)ICs/RCCAs [1,4], the Ge containing RM (Nb)IC/RCCA arc cast alloy ZF9 (Nb–24Ti–18Si–5Al–5Cr-5Ge-5Hf, at.%, nominal [36] and the RM(Nb)IC alloy ZF5 (Nb–24Ti–18Si–5Al-5Ge, at. %, nominal [37]), the RM(Nb)IC arc cast alloy JG3 (Nb–24Ti–18Si–5Al–5Cr–2Mo, at.%, nominal, [38]) and the arc cast alloy EZ5 (Nb–24Ti–18Si–5Al-5Hf-5Sn, at.%, nominal, [39]).

Fig. 7(a) and (b) plot the creep strain versus time corresponding to 1050 °C–1200 °C, respectively in case of the first creep test. Fig. 7(d) and

(e) plot the creep strain versus time corresponding to 1200 °C–1050 °C, respectively and refer to the second creep test. In both cases it can be observed that steady-state prevails with a negligible occurrence of primary creep. The steady-state creep rates were calculated in Fig. 7(a) and (b) and Fig. 7(d) and (e) and plotted in a log-log plot in Fig. 7(c) and (f) respectively, from which the stress exponent (n) can be obtained. For creep tests performed at 1050 °C, n ~2.62 for the first creep test (1050 °C first, followed by 1200 °C) and n ~ 1.73 for the second creep test (1200 °C first, followed by 1050 °C). For creep tests performed at 1200 °C, n ~1.96 for the second creep test and n ~1.66 for the first creep test.

The stress exponent n of Nb_5Si_3 is about 1, higher for Nb and Nb_{ss} [18], between 2.5 and 3 for binary Nb–10Si and Nb–16Si alloys, in a wider range from about 1.1 to 11 for Nb–Si–Ti-Hf silicide based alloys [40], in the range 2–6 for MASC and MASC based alloys (the Nb–25Ti–16Si-8Hf-2Al–2Cr alloy (nominal, at.%) is known as MASC = metal and silicide composite) and in the range 1.3–4.5 for Nb-silicide based alloys with/without Ti, and RM (Mo,Ta,W) additions and in the range 4.35–6.35 for the single crystal superalloy CMSX4 [41]. The aforementioned is from compressive creep tests of phases and alloys that were creep tested in the as cast (arc melted or directionally solidified) or heat treated conditions and were not tested using ETMT.

The n values of the alloy of this work are close to those of binary Nb_5Si_3 and Nb–Si binary alloys discussed in Ref. [40], and some of the RM(Nb)ICs studied in the ULTMAT project [41]. The n values are also close to those of the $NbCr_2$ Laves phase and A15-Nb_3Al intermetallic [18], which can be present in the microstructures of RM(Nb)ICs and RM (Nb)ICs/RCCAs [1,13]. Differences in n values of RMICs are attributed to differences in chemical composition, microstructure or both. For example, the microstructures of the above mentioned binary Nb–Si alloys consist of large primary Nb_{ss} grains surrounded by Nb_{ss} + Nb_5Si_3 eutectic, the microstructures of Nb–Si–Ti–Al–Cr-Hf silicide based alloys comprise continuous or near continuous Nb_{ss} with dispersed silicides and Laves phase or both depending on alloy chemical composition. Furthermore, the n value of RM(Nb)ICs changes with vol% silicide [40].

The alloy of this study does not meet the creep property goal (i.e., the creep strength should be greater than 170 MPa at a creep rate of 2 × 10^{-8} s^{-1} at 1200 °C). This goal assumes ρ = 7 g/cm^3 [1]) as its creep rate at 1200 °C/170 MPa was 1.75 10^{-4} s^{-1}. Also, its creep rate was higher than that of the Ti containing RM(Nb)ICs discussed in Ref. [1], as would be expected owing to its higher Ti/Si ratio (0.87). At 1200 °C/100 MPa the creep rate (1.6 10^{-6} s^{-1}) of the FAST alloy calculated with NICE [18] from the contributions made to creep by intrinsic resistances to dislocation motion [1,18] was similar to the experimental creep rate of the MASC alloy [40] but the value from the ETMT test (6.7 10^{-5} s^{-1}) was one order higher. For the creep at 1050 °C/200 MPa the alloy methodology NICE indicated a key role for the parameter δ that depends on atomic size, as the calculated (for intrinsic resistance to dislocation motion) and measured creep rates were the same (7.35 10^{-6} s^{-1}). The compressive creep test of single crystal CMSX4 at 1093 °C/200 MPa was 1.1 10^{-6} s^{-1} [41].

4. Conclusions

This study has demonstrated the use of FAST as part of a production route for Nb-silicide based alloys that are under development for applications in future high temperature turbine engines, and demonstrated that larger scale FAST processing than seen previously in the literature (i) can create fully dense, 60 mm diameter samples, (ii) brings new opportunities for scaling up production and (iii) allows for more extensive assessment of mechanical properties. In this study the compressive creep of a RMIC was evaluated for the first time using ETMT. The microstructure of the alloy after FAST, which is comprised of bcc Nb_{ss} and tetragonal αNb_5Si_3, was more homogenous compared with the cast alloy, with some interstitial contamination that occurred during powder production. The latter highlighted the importance of better control of processing conditions during milling of ingots. The FAST alloy had lower density than state of the art Ni-based superalloys and RCCAs and RHEAs, and its yield strength and specific yield strength was higher than those of the latter metallic UHTMs and comparable to those of RM (Nb)ICs and RM(Nb)ICs/RCCAs with B addition. The stress exponent n in compressive creep was in the range 1.7–2.6, similar to that of binary Nb–Si alloys and its creep rate at 1200 °C and 100 MPa was similar to that of the MASC alloy. Like the latter, the creep of the FAST alloy did not meet the creep goal.

Data availability

The raw/processed data required to reproduce these findings cannot be shared at this time as the data also forms part of an ongoing study.

Declaration of competing interest

The authors declare that they have no known competing financial

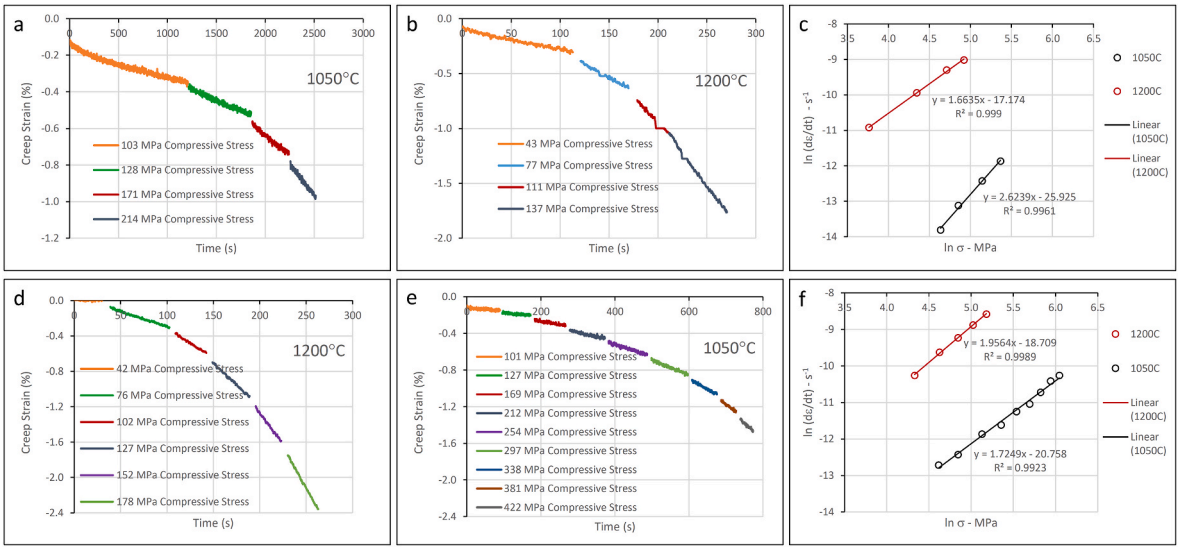

Fig. 7. Compressive creep data of matchstick specimens at elevated temperatures during ETMT testing of the Nb-silicide alloy of this work. (a) to (c) first creep experiment and (d) to (f) second creep experiment (see section 2). (a), (b), (d) and (e) creep strain versus time, (c) and (f) ln(dε/dt) versus lnσ.

interests or personal relationships that could have appeared to influence the work reported in this paper.

Acknowledgements

This work was supported by Rolls-Royce plc. and the Engineering and Physical Sciences Research Council (EPSRC) through grants EP/P006566/1: 'MAPP: EPSRC Future Manufacturing Hub in Manufacture using Advanced Powder Processes' and EP/R00661X/1 for the FAST/SPS capability as part of the Henry Royce Institute.For the purpose of open access, the author has applied a Creative Commons Attribution (CC BY) licence to any Author Accepted Manuscript version arising from this submission.

References

[1] Tsakiropoulos P. Alloys for application at ultra-high temperatures: Nb-silicide in situ composites. Prog Mater Sci 2022;123:100714. https://doi.org/10.1016/j.pmatsci.2020.100714.
[2] Senkov ON, Tsakiropoulos P, Couzinié J-P. Special issue "advanced refractory alloys": metals. MDPI. Metals 2022;12:333. https://doi.org/10.3390/met12020333.
[3] Drawin S, Justin JF. Advanced lightweight silicide and nitride based materials for turbo-engine applications. AerospaceLab 2011;3.
[4] Tsakiropoulos P. Refractory metal intermetallic composites, high-entropy alloys, and complex concentrated alloys: a route to selecting substrate alloys and bond coat alloys for environmental coatings'. Materials 2022;15:2832.
[5] Vellios N, Tsakiropoulos P. 'The effect of Fe addition in the RM(Nb)IC alloy Nb–30Ti–10Si–2Al–5Cr–3Fe–5Sn–2Hf (at.%) on its microstructure, complex concentrated and high entropy phases, pest oxidation, strength and contamination with oxygen, and a comparison with other RM(Nb)ICs, refractory complex concentrated alloys (RCCAs) and refractory high entropy alloys. Materials 2022;15:5815.
[6] Tsakiropoulos P. On the stability of complex concentrated (CC)/High entropy (HE) solid solutions and the contamination with oxygen of solid solutions in refractory metal intermetallic composites (RM(Nb)ICs) and refractory complex concentrated alloys (RCCAs). Materials 2022;15(23):8479. https://doi.org/10.3390/ma15238479.
[7] Kimura Y, Mishima Y, Yamaoka H, Sekido N. Processing, microstructure, and mechanical properties of (Nb)/Nb5Si3 two-phase alloys. Metall Mater Trans A 2005;36(3):483–8. https://doi.org/10.1007/s11661-005-0161-9.
[8] Bewlay BP, Jackson MR, Subramanian PR, Zhao J-C. A review of very-high-temperature Nb-silicide-based composites. Metall Mater Trans A 2003;34(10):2043–52. https://doi.org/10.1007/s11661-003-0269-8.
[9] Tsakiropoulos P. On the macrosegregation of silicon in niobium silicide based alloys. Intermetallics 2014;55:95–101.
[10] Weston NS, Thomas B, Jackson M. Processing metal powders via field assisted sintering technology (FAST): a critical review. Mater Sci Technol 2019;35(11):1306–28. https://doi.org/10.1080/02670836.2019.1620538.
[11] Murakami T, et al. Microstructure, mechanical properties and oxidation behavior of powder compacts of the Nb–Si–B system prepared by spark plasma sintering. Intermetallics 1999;7(9):1043–8. https://doi.org/10.1016/S0966-9795(99)00017-5.
[12] Drawin S, Monchoux JP, Raviart JL, Couret A. Microstructural properties of Nb-Si based alloys manufactured by powder metallurgy. Adv Mater Res 2011;278:533–8. https://dx.doi.org/10.4028/www.scientific.net/AMR.278.533.
[13] Guo Y, Jia L, Kong B, Zhang S, Sha J, Zhang H. Microstructure transition from lamellar eutectic to anomalous eutectic of Nb-Si based alloy powders by heat treatment and spark plasma sintering. J Alloys Compd Mar. 2017;696:516–21. https://doi.org/10.1016/j.jallcom.2016.11.236.
[14] Murakami T, Sasaki S, Ichikawa K, Kitahara A. Oxidation resistance of powder compacts of the Nb–Si–Cr system and Nb3Si5Al2 matrix compacts prepared by spark plasma sintering. Intermetallics 2001;9(7):629–35. https://doi.org/10.1016/S0966-9795(01)00043-7.
[15] Liao J, Fei T, Li Y, Yu Y, Sha J. A comparison study on microstructures and fracture behaviours of a single NbSS solid solution alloy and a two-phase NbSS/Nb5Si3 alloy prepared by spark plasma sintering and arc melting. Mater Char 2021;178:111259. https://doi.org/10.1016/j.matchar.2021.111259.
[16] Ilevbare G. INL advanced manufacturing capabilities. Idaho National Laboratory; 2022. Accessed: May 03, 2023. [Online]. Available: https://inldigitallibrary.inl.gov/sites/sti/sti/Sort_63335.pdf.
[17] Schlesinger ME, Okamoto H, Gokhale AB, Abbaschian R. The Nb-Si (Niobium-Silicon) system. J Phase Equil Aug. 1993;14(4):502–9. https://doi.org/10.1007/BF02671971.
[18] Tsakiropoulos P. On Nb silicide based alloys: alloy design and selection. Materials May 2018;11(5):844. https://doi.org/10.3390/ma11050844.
[19] Bewlay BP, Sitzman SD, Brewer LN, Jackson MR. Analyses of eutectoid phase transformations in Nb–silicide in situ composites. Microsc Microanal Aug. 2004;10(4):470–80. https://doi.org/10.1017/S1431927604040760.
[20] Ghosh G, Olson GB. Integrated design of Nb-based superalloys: ab initio calculations, computational thermodynamics and kinetics, and experimental results. Acta Mater Jun. 2007;55(10):3281–303. https://doi.org/10.1016/j.actamat.2007.01.036.
[21] Roebuck B, Cox DC, Reed RC. An innovative device for the mechanical testing of miniature specimens of superalloys. In: Superalloys 2004 (tenth international symposium). TMS; 2004. p. 523–8. https://doi.org/10.7449/2004/Superalloys_2004_523_528.
[22] Roebuck B, Cox D, Reed R. The temperature dependence of γ′ volume fraction in a Ni-based single crystal superalloy from resistivity measurements Feb. 2000;44(6).
[23] Sutton G, Greenen A, Roebuck B, Machin G. Imaging phosphor thermometry from T = 20 °C to 450 °C using the time-domain intensity ratio technique. Meas Sci Technol Apr. 2019;30(4):044002. https://doi.org/10.1088/1361-6501/ab04ea.
[24] Sulzer S, Alabort E, Németh A, Roebuck B, Reed R. On the rapid assessment of mechanical behavior of a prototype nickel-based superalloy using small-scale testing. Metall Mater Trans A Sep. 2018;49(9):4214–35. https://doi.org/10.1007/s11661-018-4673-5.
[25] Roebuck B, Brooks M, Pearce A. Good practice guide for miniature ETMT tests, NPL good practice guide No. 137. National Physical Laboratory; Jan. 2016.
[26] D'Souza N, Roebuck B, Collins DM, West GD, Panwisawas C. Relating micro-segregation to site specific high temperature deformation in single crystal nickel-base superalloy castings. Mater Sci Eng, A Jan. 2020;773:138862. https://doi.org/10.1016/j.msea.2019.138862.
[27] D'Souza N, Hardy MC, Roebuck B, Li W, West GD, Collins DM. On the rate dependence of precipitate formation and dissolution in a nickel-base superalloy. Metall Mater Trans A 2022;53(7):2480–95. https://doi.org/10.1007/s11661-022-06680-8.
[28] Perry SJ, D'Souza N, Collins DM, Roebuck B, Dong HB. An in situ resistance-based method for tracking the temporal evolution of recovery and recrystallization in Ni-base single-crystal superalloy at super-solvus temperatures. Metall Mater Trans A May 2023;54(5):1582–96. https://doi.org/10.1007/s11661-022-06861-5.
[29] Massalski TB, Okamoto H, Subramanian PR, Kacprzak L, editors. Binary alloy phase diagrams. second ed. Materials Park, OH: ASM International; 1990. p. 2748–9.
[30] Vellios N, Tsakiropoulos P. 'The effect of Fe addition in the RM(Nb)IC alloy Nb–30Ti–10Si–2Al–5Cr–3Fe–5Sn–2Hf (at.%) on its microstructure, complex concentrated and high entropy phases, pest oxidation, strength and contamination with oxygen, and a comparison with other RM(Nb)ICs, refractory complex concentrated alloys (RCCAs) and refractory high entropy alloys. (RHEAs)', Mater 2022;15(17):5815. https://doi.org/10.3390/ma15175815.
[31] Koch CC, Scarbrough JO, Kroeger DM. Effects of interstitial oxygen on the superconductivity of niobium. Phys Rev B Feb. 1974;9(3):888–97. https://doi.org/10.1103/PhysRevB.9.888.
[32] Gallagher E. "Processing of Nb-Si alloys using mixed elemental and pre-alloyed powders". The University of Sheffield; 2023.
[33] McCaughey C, Tsakiropoulos P. 'Type of primary Nb5Si3 and precipitation of Nbss in αNb5Si3 in a Nb-8.3Ti-21.1Si-5.4Mo-4W-0.7Hf (at.%) near eutectic Nb-Silicide-Based alloy'. Materials 2018;11(6):967. https://doi.org/10.3390/ma11060967.
[34] Zacharis E, Utton C, Tsakiropoulos P. A study of the effects of Hf and Sn on the microstructure, hardness and oxidation of Nb-18Si silicide based alloys without Ti addition. Materials 2018;11(12):2447. https://doi.org/10.3390/ma11122447.
[35] Senkov ON, Miracle DB, Chaput KJ. Development and exploration of refractory High entropy alloys—a review. J Mater Res 2018;33:3092–128.
[36] Li Z, Tsakiropoulos P. On the microstructure and hardness of the Nb-24Ti-18Si-5Al-5Cr-5Ge and Nb-24Ti-18Si-5Al-5Cr-5Ge-5Hf (at.%) silicide based alloys. Materials 2019;12:2655.
[37] Li Z, Tsakiropoulos P. The microstructure of Nb-18Si-5Ge-5Al and Nb-24Ti-18Si-5Ge-5Al *in situ* composites. J Alloys Compd 2013;550:553–60.
[38] Geng J, Tsakiropoulos P. A study of the microstructures and oxidation of Nb-Si-CrAl-Mo *in situ* composites alloyed with Ti, Hf and Sn. Intermetallics 2007;15:382–95.
[39] Zacharis E, Utton C, Tsakiropoulos P. A study of the effects of Hf and Sn on the microstructure, hardness and oxidation of Nb-18Si silicide-based alloys-RM(Nb)ICs with Ti addition and comparison with refractory complex concentrated alloys (RCCAs). Materials 2022;15:4596.
[40] Chan Kwai S. Modelling creep behaviour of niobium silicide in-situ composites. Mater Sci Eng 2002;A337:59–66.
[41] Ultra high temperature materials for turbines-ULTMAT. Specific targeted research project (STREP) in the FP6 EU framework, contract: AST3-CT-2003-502977, compressive creep data for RMICs and CMSX4, interim report. 2005.